Solar RRL
www.solar-rrl.com

Attitude Determination in Space with Ambient Light Sensors using Machine Learning for Solar Cell Characterization

*Lennart K. Reb, Michael Böhmer, Benjamin Predeschly, Lukas V. Spanier, Christoph Dreißigacker, Andreas Meyer, and Peter Müller-Buschbaum**

Exploration of novel thin-film solar cell technologies outreaches for their application in space. For extraterrestrial tests, irradiance conditions must be well determined to extract quantitative solar cell performances. Here, a new method for solar position determination is presented, based on parallelized ambient light sensor measurements is presented obtained from the sounding rocket experiment Organic and Hybrid Solar Cells In Space during the MAPHEUS-8 mission. The solar position evolution is optimized using stochastic and gradient-based methods in a Bayesian approach. Comparison with independent positioning estimates shows compelling agreement, lying mostly within 5° deviation. The inclusion of a simple Earth irradiation component mitigates a small systematic offset. Further, solution uncertainties are estimated with Monte-Carlo Markov-chain sampling. The point-source irradiation model's accuracy can compete with that of a camera-based trajectory. During equatorial Sun positions, the method's precision appears even higher—the 1σ uncertainty of the derived solar position is as small as 3° for the effective angular deviation. This simple sensor array triangulation method being complementary to other attitude determination methods shows reasonable accuracies and allows implementation in systems of limited computational capabilities to determine the solar position or irradiance conditions for space or terrestrial solar cell applications.

1. Introduction

Solar cell technologies play a steadily increasing role in the energy transition in recent years, however, they have been used already in the early 1960s of the past century for generating power in space.[1–3] Today, they are widely applied for power delivery in spacecrafts, satellites, and probes, where the field is dominated by silicon photovoltaics and high-efficiency multi-junction devices based on GaAs or related materials.[4–7] Within the past decade, novel thin-film materials and technologies were discovered that have been improved continuously by systematic research ever since.[8,9] In particular, next-generation solar cell technologies, which are based on soft materials such as hybrid organic–inorganic perovskites or organic semiconducting polymers, offer a variety of new options and features that make them particularly interesting for their application in space.[10,11] Here, key advantages are based on their significantly reduced thickness of (sub-)micrometer scale, compared to current space solar cells, which are significantly thicker.[12] Thereby significantly higher specific powers of the solar modules can be envisioned when using hybrid organic–inorganic perovskites or organic semiconducting polymers. Moreover, their upscalable manufacturing at low- or ambient temperatures from solution enables the use of thin polymeric foils as substrates and thereby true mechanical

L. K. Reb, B. Predeschly, L. V. Spanier, P. Müller-Buschbaum
Lehrstuhl für Funktionelle Materialien
Physik Department
Technische Universität München
85748 Garching, Germany
E-mail: muellerb@ph.tum.de

The ORCID identification number(s) for the author(s) of this article can be found under https://doi.org/10.1002/solr.202200537.

[+]Present address: Projects and Techniques Division, Institut Laue-Langevin, 38042 Grenoble, France

© 2022 The Authors. Solar RRL published by Wiley-VCH GmbH. This is an open access article under the terms of the Creative Commons Attribution-NonCommercial License, which permits use, distribution and reproduction in any medium, provided the original work is properly cited and is not used for commercial purposes.

DOI: 10.1002/solr.202200537

M. Böhmer
Zentrales Technologielabor
Physik Department
Technische Universität München
85748 Garching, Germany

C. Dreißigacker, A. Meyer[+]
Institut für Materialphysik im Weltraum
Deutsches Zentrum für Luft- und Raumfahrt (DLR)
51147 Köln, Germany

P. Müller-Buschbaum
Heinz Maier-Leibnitz Zentrum (MLZ)
Technische Universität München
85748 Garching, Germany

Check for updates
2367198x, 2022, 11, Downloaded from https://onlinelibrary.wiley.com/doi/10.1002/solr.202200537 by Dtsch Zentrum F. Luft-U. Raum Fahrt In D. Helmholtz Gemein., Wiley Online Library on [09/02/2023]. See the Terms and Conditions (https://onlinelibrary.wiley.com/terms-and-conditions) on Wiley Online Library for rules of use; OA articles are governed by the applicable Creative Commons License

flexibility of such ultra-thin and lightweight devices.[13–19] Research on their long-term stability came increasingly into focus in the past years, and the novel material attests to promising behavior in harsh environments of strong particle irradiation.[20,21] Taking these novelties together, the technologies have the potential to become the next generation of space solar cells.[22,23] Previous tests of the novel materials range from laboratory tests that simulate space conditions, over near-space missions on stratospheric balloon flights to rocket flights to space.[24–30] However, further tests that focus on their application in their designated role are necessary before these next-generation solar cells can make the step from experimental technologies to their integration as conventional space technologies. In contrast to laboratory or terrestrial experiments, the determination of solar cell irradiation in a space environment is the central challenge in relating the solar cell behavior to the solar irradiance and thereby quantifying solar cell performance parameters. For terrestrial applications, there exists a broad range of different methods that allow determining the solar position or at least rotating the solar panel to follow the solar movement via feedback loops.[31] Precise attitude control in space, however, raises the necessity for testing further methods such as camera-based methods for determining the Earth horizon.[32] Toward low-cost solar position determination, the current of multiple solar cells in the orthogonal arrangement has been measured to successfully derive the angular position of the light source.[33] However, their low number of sensing surfaces and orientations result in limited angular estimation accuracy and a limited field of view.

In the present study, we present a method for solar position determination based on triangulation via data parallelization of several ambient light sensors. Each sensor is a simple, commercially available I2C sensor and faces in a distinct direction into space. In our work, we analyze the measurement data obtained by the light sensors being part of the Organic and Hybrid Solar Cells in Space (OHSCIS) sounding rocket module, which we designed and used to successfully test novel thin-film solar cell technologies in the space environment for the very first time during the sounding rocket flight of MAPHEUS-8.[27,28] The triangulation method we describe here can readily be generalized to any geometrical arrangement of ambient light sensors and is not restricted to extraterrestrial use for solar positioning or light irradiance determination. We investigate the time-synchronized light sensor measurements by establishing and refining a solar irradiation model using machine learning techniques to derive a global solution for the global model parameters and the solar position at each time. Making use of posterior Monte-Carlo Markov-Chain (MCMC) sampling, we estimate model parameter distributions and correlations as well as solar position estimation errors for each measurement. In recent work, Braun et al. reconstructed the payload orientation over time by detecting the Earth's horizon and Sun on the images from two opposite-looking cameras and fusing the resulting estimates of the Earth nadir and Sun direction vectors with time-integrated measurements from an inertial measurement unit (IMU).[32] Comparing both datasets, we find strong agreement between both trajectories with an absolute deviation of only a few degrees within the entire dataset. We further show that including a simple Earth model of a homogeneously radiating, Lambertian extended surface as a second radiation component improves our trajectory solution by increasing the total model likelihood, reducing the attributed measurement noise, and confining the model results closer to the trajectory reconstructed by Braun et al. From the model, we derive the evolution of Earth's normal direction over time, which allows a rough but fully defined orientation estimate by fixing the third independent axis of rotation. The derived model results allow triangulating the solar position over time and thus reconstructing the irradiance conditions that have been present during MAPHEUS-8. Potential future flights of the OHSCIS module, as well as independent systems relying on parallelized ambient light sensors, can be based on this principle for light-source positioning or solar irradiance determination.

2. Experiment and Dataset

The OHSCIS module (Figure S1a, Supporting Information) contained eight hatches each 45° azimuthally arranged. They were covered with fused silica glass ($n = 1.46$ at $\lambda = 550$ nm) that has negligible absorption in the visible range but gives rise to angular-dependent Fresnel reflection. Each hatch contained two ambient light sensors of type BH1750FVI that steadily collect illumination measurements during the flight (Figure S1b, Supporting Information).[33] The special feature of the two sensors that are located in a single hatch is that one sensor is rotated upwards by 22.5° and the other one downwards by 22.5° as indicated in Figure S1c, Supporting Information, creating an effective viewing angle of 45° between the two sensors. In combination with the eight hatches with the 45° angle between neighboring hatches, each of the total 16 light sensors of the OHSCIS module was oriented in a distinct spatial direction.

The light sensors are designed for terrestrial illumination measurement purposes and thus are expected to saturate under strong AM0 irradiation, the solar irradiation spectrum with around 1366 W m^{-2} in space, according to the ASTM E-490 spectrum.[34,35] To quantify expected saturation, the sensor spectral sensitivity curve extracted from the sensor datasheet was folded with the AM0 solar spectrum, which results in possible maximum brightness measurements of 88 331 lx in the sensor configuration of lowest sensitivity (default high-brightness measurement-time register value of 31), while the 16-bit measurement range is effectively limited to 65 535 lx.[33] Thus, the measurement-time register value was further reduced down to 15 to avoid possible saturation for the sensor application in space with a safety margin of around 1/3 of the available measurement range as a compromise of safety and proper use of large parts of the possible sensitivity scale for accurate measurements. **Figure 1**a shows the linearity of the measurement-time register value to sensor brightness response for stable light sources in our laboratory. Here, we note that this graph and the results of this work allows to fine-tune the measurement-time register value for improved accuracy for future flights of the OHSCIS module.

In this work the focus lies on the sensor measurements acquired during stable payload configuration, i.e., selecting approximately the μ-gravity time of the flight of MAPHEUS-8. During flight, the cameras could capture both, the Sun and Earth horizon, even simultaneously, which was not possible in earlier flights.[32] Good solar position and Earth horizon tracking at different times of the flight by the cameras have been the key to

© 2022 The Authors. Solar RRL published by Wiley-VCH GmbH

2367198x, 2022, 11, Downloaded from https://onlinelibrary.wiley.com/doi/10.1002/solr.202200537 by Dtsch Zentrum F. Luft-U. Raum Fahrt In D. Helmholtz Gemein., Wiley Online Library on [09/02/2023]. See the Terms and Conditions (https://onlinelibrary.wiley.com/terms-and-conditions) on Wiley Online Library for rules of use; OA articles are governed by the applicable Creative Commons License

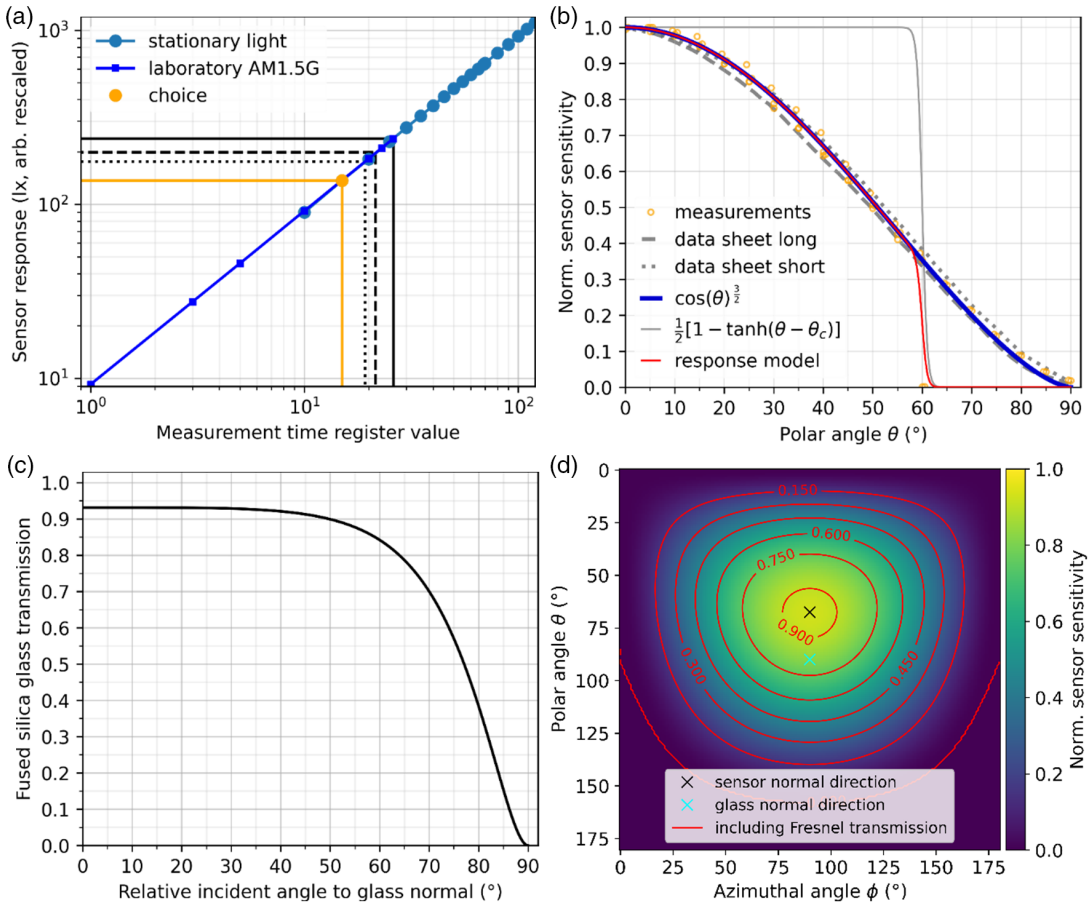

Figure 1. Light sensor properties and angular response modeling. a) Measured linear correlation of sensor measurement time and response for ambient light and a strong laboratory light source. The black solid line shows the maximum register value that can be used without causing sensor saturation in laboratory AM1.5G measurements. The dashed black line shows the maximum register value that can be used for AM0 without saturation from folding the AM0 spectrum with the spectral sensor response. The dotted black line results from scaling the saturation register threshold measured with the AM1.5G lamp to the AM0 spectrum. The solid orange line is the choice for the space flight with a 1/3 safety margin. Note the double-logarithmic representation. b) Angular light sensor response as measured in the lab, extracted from manufacturer datasheet, and approximated with a cosine to the power of 3/2 (blue). On top we add the sigmoidal function that suppresses the response above the cutoff angle α_c, resulting in the total sensor response model (red). c) Angular fused silica transmission derived from Fresnel equations for $n = 1.46$. d) Effective sensor response angular contour plot including sensor response (without sigmoidal function) and Fresnel transmission. The contour lines are no circles since the glass transmission peaks at angles different than the peak of the sensor sensitivity and due to the cylindrical Mercator projection that distorts regions at high latitudes.

the high precision of attitude determination in Braun et al.'s work. This in turn is the solid ground to interpret the results of this work. The dataset includes all light sensor measurements starting with the first at around $T + 60.5$ s (after lift-off) after activation of the rate-control system. The measurement at $T + 444.4$ s was included as the last measurement, before payload spin-up became too strong, yielding a total number of 256 measurements of all 16 sensors that are time-synchronized. This way as many reliable measurements as available were included with the goal to maximize the amount of data for model training. As a convention in this work, each of the 256 measurements is called (single) frame. For the selected data, the payload showed a sufficiently stable orientation, i.e., within the measurement time asynchrony of the 16 light sensors (of up to 0.7 s in the dataset), the payload orientation change effective angle is strictly below 1°.[28] Thus this did not influence the solar triangulation results within their accuracy. Each single sensor measurement in the dataset is an integer number ranging from 0 to 31 776, the minimum and maximum registered brightness value by a light sensor during flight.

3. Radiation Model

To model the brightness values measured by the sensors, we need: a) to define the sensor response function, b) consider further effects that have an impact on the model, e.g., angle-dependent fused silica transmission or geometrical shadowing of the light sensors, and c) to incorporate all these relations into a coordinate system together with the definition of the light source(s).

We describe the sensor sensitivity as a function of the incident angle onto the sensor, which is measured relative to the sensor surface normal or sensor viewing direction. To find a functional dependence of incident angle and sensor response, we extract the

© 2022 The Authors. Solar RRL published by Wiley-VCH GmbH

2367198x, 2022, 11, Downloaded from https://onlinelibrary.wiley.com/doi/10.1002/solr.202200537 by Dtsch Zentrum F. Luft-U. Raum Fahrt In D. Helmholtz Gemein., Wiley Online Library on [09/02/2023]. See the Terms and Conditions (https://onlinelibrary.wiley.com/terms-and-conditions) on Wiley Online Library for rules of use; OA articles are governed by the applicable Creative Commons License

sensor sensitivity curves from the sensor datasheet for vertical and horizontal directions and execute laboratory measurements for various incident angles with the light sensors in our labs with a fixed and stable light source (Figure 1b). Comparing the extracted and measured sensor sensitivity curves, we find a good agreement within a few degrees or percent, which is our attributed measurement error of single sensor measurements. The validation measurements lie in between the range of the curves extracted from the datasheet. The empirical and extracted data show a strong agreement with a cosine function to the power of 3/2. Therefore, for numerical simplification in our calculations, we model the sensor sensitivity curve like that as

$$R_{\mathrm{S}}(\alpha) = \cos(\alpha)^{3/2} \tag{1}$$

with the incident angle α. Deviations in the shape of our simplified sensor model and the intrinsic functional behavior are small, however, there might be systematic sensor misalignment properties that we estimate to be of order 1°. In our laboratory tests, we could not detect inter-sensor sensitivity variations, however, such systematic sensitivity sensor differences would add to measurement uncertainty. Also, sensor read-out noise adds on top to the measurement uncertainty. For AM1.5G 1000 W m^{-2} irradiance, we determine a standard measurement error of 0.1%. However, the effective measurement error can become more pronounced for lower signal-to-noise ratios in faint conditions. All these effects add up to potential measurement uncertainties that we discuss in the next section.

A closer look at the measurements in Figure 1b shows a quick cutoff of the sensor response caused by the onset of geometrical shadowing effects above certain incident angles. Here, we note that this effect occurs due to shadowing by the rocket payload, i.e., only in one direction along the vertical axis for a sensor. To include this cutoff behavior in the modeling in an easy way, we define the cutoff angle α_{c} to be identical in all directions and extend the sensor response model with a sigmoidal function

$$R_{\mathrm{S,eff}}(\alpha) = \cos(\alpha)^{3/2}\mathrm{Sig}(\alpha, \alpha_{\mathrm{c}}) \tag{2}$$

where the sigmoidal function

$$\mathrm{Sig}(\alpha, \alpha_{\mathrm{c}}) = \frac{1}{2}\left\{1 + \tanh\left[\frac{\gamma(\alpha - \alpha_{\mathrm{c}})}{2}\right]\right\} \tag{3}$$

is defined to be close to 1 below α_{c}, 0.5 at α_{c}, and close to 0 above α_{c} (cf. Figure 1b) with the slope γ. We use the sigmoidal function instead of, e.g., a Heavyside step function to be compatible with gradient-based optimization methods. We set $\gamma = 0.88$ to let the sigmoidal function decrease from 0.9 to 0.1 within 5°, which roughly corresponds to the estimated geometrical shadowing range.

A light ray is transmitted through the glass before arriving at the sensor. The glass transmission follows Fresnel's equations since glass absorption is negligible in the optical range, where the solar spectrum and sensor sensitivity peak (≈550 nm, see Figure S2, Supporting Information). Correspondingly, we use a refractive index of fused silica of $n = 1.46$.[36] The effective glass reflection coefficients of light of different polarization concerning the plane of incidence are

$$R_{\perp} = \left[\frac{n_1\cos(\alpha_1) - n_2\cos(\alpha_2)}{n_1\cos(\alpha_1) + n_2\cos(\alpha_2)}\right]^2 \tag{4}$$

$$R_{\parallel} = \left[\frac{n_2\cos(\alpha_1) - n_1\cos(\alpha_2)}{n_2\cos(\alpha_1) + n_1\cos(\alpha_2)}\right]^2 \tag{5}$$

where n_1 and α_1 are the refractive index and incident angle (to the surface normal) of a light ray inside the initial medium, n_2 and α_2 in the final medium, respectively. Since for the transmission from vacuum to glass and back from glass to vacuum n_1 and n_2, as well as α_1 and α_2, are exchanged, respectively, and the expressions for $R_{\perp}, R_{\parallel}$ are squared and hence symmetric functions, we can write the effective glass transmission as

$$T = \left(1 - \frac{R_{\perp} + R_{\parallel}}{2}\right)^2 \tag{6}$$

The refracted angle we express via Snell's law via incident angle and the refractive indices

$$\alpha_2 = \arcsin\left[\frac{n_1\sin(\alpha_1)}{n_2}\right] \tag{7}$$

and thus derive the angle-dependent fused silica transmission $T(\alpha_1)$ in Figure 1c. Note that the incident angle of the light ray on the glass differs from the incident angle of the sensor. For the description of the geometry, we use a spherical coordinate system to make use of the azimuthal symmetry of the OHSCIS module to define a certain direction with the azimuthal angle φ and the polar angle θ

$$\mathbf{r}(\varphi, \theta) = \begin{pmatrix}\cos(\varphi)\sin(\theta)\\ \sin(\varphi)\sin(\theta)\\ \cos(\theta)\end{pmatrix} \tag{8}$$

We define the coordinate system following the MORABA coordinate system, i.e., the payload points always toward $\theta = 0°$, a radial direction of the cylindrical OHSCIS module mantle surface corresponds to $\theta = 90°$, see also Figure S3, Supporting Information. Thus, the eight window normal directions are $(\varphi_i, \theta_i) = (16.875^{\circ} + 45^{\circ}\cdot i, 90^{\circ})$ with i being an integer. Accordingly, the sensor φ_i coordinates are the same, $\theta_i = 67.5^{\circ}, 112.5^{\circ}$ for upward- and downward-oriented light sensors, respectively. First, we consider a point source defined by its position $\mathbf{r}$. The effective incident angle between a ray direction $\mathbf{r}$ and surface normal direction $\mathbf{n}$ is then calculated via the scalar product

$$\alpha = \arccos\left(\frac{\mathbf{r}\cdot\mathbf{n}}{|\mathbf{r}||\mathbf{n}|}\right) \tag{9}$$

Combining Equations (2)–(7) to account for total solar brightness, sensor angular sensitivity, shadowing effects, and angular-dependent glass transmission, we calculate the response of a specific sensor to the light source as

$$\begin{aligned} R_{\mathrm{total}}\left(A, \alpha_c, \mathbf{n_s}, \mathbf{n_g}, \mathbf{r}\right) &= R_{\mathrm{total}}\left(A, \alpha_{\mathrm{c}}, \varphi_{\mathrm{s}}, \theta_{\mathrm{s}}, \varphi_{\mathrm{g}}, \theta_{\mathrm{g}}, \varphi, \theta\right) \\ &= LR_{\mathrm{s}}(\alpha_{\mathrm{s}})\mathrm{Sig}(\alpha_{\mathrm{s}}, \alpha_{\mathrm{c}})T\left(\alpha_{\mathrm{g}}\right) \end{aligned} \tag{10}$$

With the sensor normal direction $\mathbf{n_s}$, glass normal direction $\mathbf{n_g}$, and the derived incident angles α_{s} and α_{g} onto a sensor

© 2022 The Authors. Solar RRL published by Wiley-VCH GmbH

2367198x, 2022, 11, Downloaded from https://onlinelibrary.wiley.com/doi/10.1002/solr.202200537 by Dtsch Zentrum F. Luft-U. Raum Fahrt In D. Helmholtz Gemein., Wiley Online Library on [09/02/2023]. See the Terms and Conditions (https://onlinelibrary.wiley.com/terms-and-conditions) on Wiley Online Library for rules of use; OA articles are governed by the applicable Creative Commons License

and the glass, respectively. Here, we introduced L, the global scaling value that refers to the brightness of the light source. An example simulation of a point source together with sensor response is shown in **Figure 2**a, which illustrates how multiple sensors can be used together for point-source triangulation. For modeling the solar irradiation (the Sun-only model) onto each of the 16 light sensors for a given solar position, we describe the Sun as a point-like light source. In reality, the Sun with its angular diameter of around 1° is an extended source. However, within fair reasoning, the solar ray divergence does not affect our model description. For a given set of parameters, L, α_c, φ, θ we calculate the sensor response for each of the 16 light sensors to obtain a sensor simulation for the given parameters that can describe a single frame.

In a refinement step for the model (Sun + Earth model), we include Earth as a second irradiation source. Earth is hereby modeled as an extended source where we apply the following assumptions (also see Figure S4, Supporting Information). First, Earth subtends a semisphere, i.e., a solid angle of 2π. Second, the semisphere is approximated by a discrete number of angularly equally distributed points, i.e., with regular spacing between them. To achieve this, we make use of the special Icosahedron, a convex regular polyhedron with 20 faces that are equilateral triangles. These points of known coordinates allow quick iterative doubling of points by creating new points in the center of nearest neighbors. The new points again produce smaller equilateral triangles. This way, we reach a reasonable number of points to describe Earth within a few iterations. Third, all these points act as point sources with equal brightness. This is equivalent to assuming Earth to be an ideal and homogeneous Lambertian emitter. Each point is contributing to the sensor response as described earlier. The orientation of the semisphere we describe with its "normal" direction $\mathbf{n_e}$. This direction is the same as the normal direction of an infinite plane that covers the very same semisphere. In other words, Earth's normal direction points toward Earth's center. We create this Earth radiation model where first, the model optimization is not sensible of its discretized nature, and second, where a change of Earth's normal direction changes Earth radiation influence of the sensors in a continuous way to enable gradient-based optimizations. We select the radiating Earth points by limiting their angular distance to the normal direction to 90° by using the sigmoidal function introduced earlier to assign weights to the Earth points (see color in Figure S4, Supporting Information). This ensures a gradual change in horizon-point weighting. Second, we notice that rotating Earth points can lead to a non-monotonic sensor signal response and thus hinders the convergence of gradient-based optimizations. Thus we decide to keep the coordinates of Earth points fixed relative to the light sensors, to avoid such discretization artifacts. We define Earth's brightness with a new parameter E that is normalized to the (weighted) number of points. This way, our model is independent of the number of Earth points used and we can use Earth's brightness as a resilient estimate parameter.

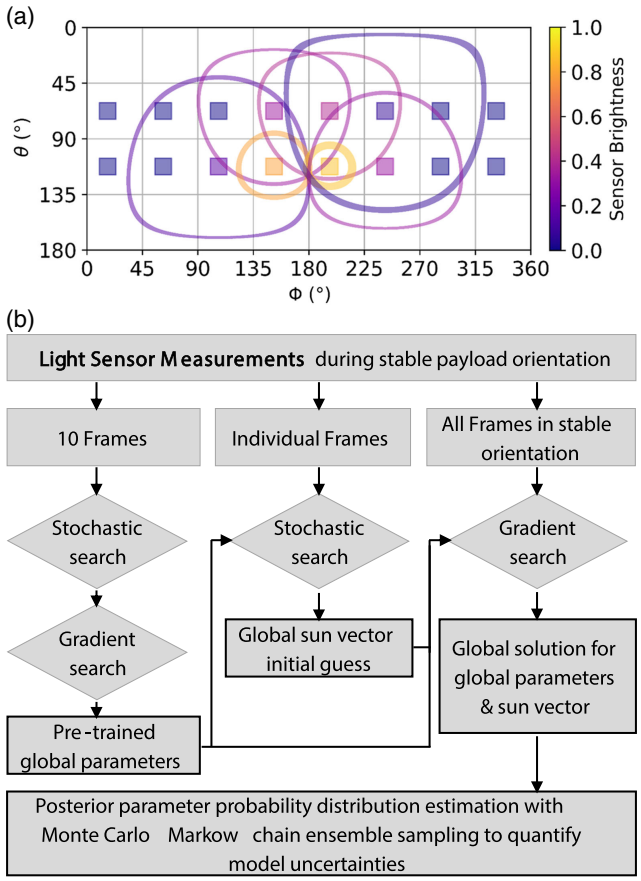

Figure 2. a) Simulation of a point source at $\varphi = 180^{\circ}$ and $\theta = 120°$ with the corresponding sensor responses. By selecting an interval of ±0.01 in the contour map in Figure 1d, each sensor response ring represents possible positions of the point source to create this individual response. At the intersection of sensor response rings, we can allocate the solar position. b) Model optimization flow diagram. The small selection of 10 frames out of the entire dataset is used to derive pre-trained model parameters. These parameters are the basis for the stochastic search of the orientation parameters in all 256 individual frames. These results enter a gradient-based global optimization run to obtain a consistent solution for all parameters simultaneously. Starting from this maximum likelihood estimate, posterior probability distribution sampling is applied to get parameter uncertainties and correlation (details see text).

To extend the Sun-only model with the Earth component, we stick to the previously described coordinate system. For the rocket flight of a few minutes, we assume a fixed effective angle of the solar position and Earth-normal direction. At apogee time, 4:25 a.m. on June 13th, 2019 in Kiruna, Sweden, the geometric solar angle above the horizon was ≈10°. Thus the effective angle between the direction of the Sun and the normal direction of Earth is $\alpha_e = \angle(\mathbf{n_e}, \mathbf{r}) \approx 100^{\circ}$. Within the time passed during the dataset, the Sun moves by an angle that roughly equals its angular diameter. Thus, we only introduce a small error by fixing the angle. A rotation of the payload around the Sun direction $\mathbf{r}$ is equivalent to a rotation of the Earth's normal vector $\mathbf{n_e}$ around the Sun direction. Thus, we describe all possible payload orientations by describing all possible Earth-normal orientations that lie on a cone around the solar position with the fixed opening angle α_e and an Earth phase angle β, which describes Earth's position on the cone. We define $\beta = 0^{\circ}$ to be eastwards and $\beta = 90^{\circ}$ to be northwards relative to the solar vector in the payload coordinate system. The advantage of defining Earth position with this Earth phase angle is that we only introduce one more angular

© 2022 The Authors. Solar RRL published by Wiley-VCH GmbH

2367198x, 2022, 11, Downloaded from https://onlinelibrary.wiley.com/doi/10.1002/solr.202200537 by Dtsch Zentrum F. Luft-U. Raum Fahrt In D. Helmholtz Gemein., Wiley Online Library on [09/02/2023]. See the Terms and Conditions (https://onlinelibrary.wiley.com/terms-and-conditions) on Wiley Online Library for rules of use; OA articles are governed by the applicable Creative Commons License

parameter for each frame in the later optimization to keep the model complexity limited. Later back transformation of the Earth's normal orientation to the payload coordinate system is straightforward and computationally fast.

Earth can be treated as a first-order perturbation of the Sun-only model. To clarify this reasoning, we consider the limiting case from basic radiative concepts. A perfectly white Lambertian disk covers the semisphere and is illuminated from a point source that is opposed to it (maximum Lambertian emission, Sun in disk surface's zenith). Then the integrated flux that is reflected from this disk and passes through a unit surface (the sensor) cannot be larger than the flux passing the surface from the initial point source. For a lower Earth Albedo and for a Sun position that is far away from Earth's zenith, Earth reflection is reduced and consequently Earth's contribution. We can estimate the magnitude of Earth brightness for a typical Earth Albedo of 0.3 and the projection effect for given geometry which scales as the sinus of solar angle above the Earth horizon, $E_{\text{exp}} \approx 0.3 \cdot \sin(10)L \approx 0.05L$. In the next step, we estimate the effective Earth radiation contribution for a sensor measurement by comparing the maximum normalized sensor response from Sun (0.93) and Earth (≈0.3) from our numerical model, including glass reflection effects. In other words, the maximum normalized single sensor response from an extended source of 2π cannot be more than 1/3 of the response from a point source. Taking these numbers together, we find that solar irradiation is significantly stronger than Earth irradiation for a single sensor and dominates orientation determination. However, in phases where solar illumination of the sensors is weak, we expect the Earth model to improve the quality of orientation estimation significantly, especially since Earth produces a smooth response curve for multiple light sensors at the same time. Based on the aforementioned reasoning, we limit the number of icosahedral splitting iterations to two, resulting in 162 Earth points that are used to model Earth in a reasonable time. In Figure S4, Supporting Information, we show a 3D visualization of the resulting Earth radiation model for Earth-normal direction pointing toward the nadir.

With this, we have defined all the important model components and end up with a set of variable global model parameters that are solar brightness L and cutoff angle α_c for the Sun-only model, plus Earth brightness E for the composite model. The noise parameter will be introduced in the following. Fixed parameters are the cutoff slope and relative angle between the Sun and Earth-normal directions. Each frame is characterized by the orientation parameters, i.e., the Sun position φ and θ for the Sun-only model, plus the Earth phase β for the composite model. The entire calculation of the model is done in a fully vectorized fashion, meaning that with all model parameters for all frames in time, we calculate the model predictions for each sensor simultaneously, which allows us to performantly create a global residual and optimize the loss function.

4. Bayesian Optimization

The entire optimization routine is implemented in Python using packages like NumPy, SciPy, pandas, emcee, LMFit, and matplotlib extensively.[37–42] To optimize the model prediction for the best resemblance of the measurement dataset we use maximum likelihood estimation (MLE) assuming normally distributed residuals. This means we assume an independent and symmetric distribution of measurement errors around their expectation value. This approach is equivalent to solving the ordinary least-squares minimization problem that also returns the MLE. In the first step, we obtain the most likely parameter solution for the employed model for the given data. On top of that, we use Bayesian posterior sampling as a second step, making use of the affine invariant MCMC to estimate the posterior probability distributions of the model parameters.[43,44] These distributions in turn allow us to consistently infer the uncertainty of the model parameters. We choose MCMC sampling to construct probability distributions for the parameters in a robust way. First, nonlinearities in the mathematical model require a careful calculation of confidence intervals of the parameter estimates. MCMC sampling converges to the true underlying probability distribution of model parameters, thus it is direct imaging of the desired objective. Second, the Monte-Carlo sampled high-dimensional parameter space contains all information required for subsequent analysis. The marginalization over certain parameters allows us to directly obtain the desired value distribution for a parameter of interest from which confidence intervals can be read-off. In addition, all model uncertainties, for example, uncertainties of the estimation of solar position are propagated automatically, i.e., they enter consistently the derivation of solar irradiance uncertainty. We do this routine twice, once for the Sun-only model and once for the model Sun + Earth as described below.

Maximizing the likelihood function is equivalent to maximizing the log-likelihood function

$$LL = \ln[L_X(\Lambda, \sigma^2)] = -\frac{n\ln(2\pi)}{2} - n\ln(\sigma) - \frac{1}{2\sigma^2}\sum_i^n (\mathbf{x_i} - \boldsymbol{\lambda_i})^2 \tag{11}$$

where n is the number of measurement frames, σ is the width of the presumed normal distribution of the residuals, $\mathbf{x_i}$ is the light sensor measurement vector consisting of the 16 measurements of the ith frame, and $\boldsymbol{\lambda_i}$ is the model prediction for the ith frame. X and Λ contain all the observations and predictions, respectively, and can be considered as matrices. The sum of the squared residuals in the last term corresponds to the objective function in least-square minimization. In the present case, the log-likelihood is the objective function that is to be maximized during the optimization routine. In practice, we use a minimization of the negative log-likelihood function, the pedant to a cost function, or internal energy for simulated annealing methods. Λ contains the entire model and here enter all parameters of the optimization. This direct definition of the model for all frames and all sensors allows simultaneous training of all global model parameters. The single-frame model prediction for the orientation, given by φ_i, θ_i, and β_i for the solar and Earth position, are independent estimations for each frame. In other words, the optimizations of the solar position of two different frames are independent of each other, however, all frames influence the global parameters with equal weighting and hence influence each other indirectly.

© 2022 The Authors. Solar RRL published by Wiley-VCH GmbH

2367198x, 2022, 11, Downloaded from https://onlinelibrary.wiley.com/doi/10.1002/solr.202200537 by Dtsch Zentrum F. Luft-U. Raum Fahrt In D. Helmholtz Gemein., Wiley Online Library on [09/02/2023]. See the Terms and Conditions (https://onlinelibrary.wiley.com/terms-and-conditions) on Wiley Online Library for rules of use; OA articles are governed by the applicable Creative Commons License

The parameter σ is a weighting parameter that describes the uncertainty of the measurements in the dataset. Into such uncertainties, we subsume all deviations from the ideal model, i.e., systematic and stochastic measurement noise of individual light sensors, absolute sensitivity scaling differences of the sensors, misalignment of the sensor orientation, timing differences between the measurement times within a single frame, model imperfections such as sensor sensitivity curve deviations. Since σ enters the optimization as an unconstrained parameter, its final value can be considered as an independent measure of the amount of model-to-measurement deviation that is left over after optimization, where a lower value signifies better matching.

In the first step of optimization, we aim at finding the global minimum of the negative log-likelihood function to derive the MLE for all parameters. To do so, we adopt an optimization routine that comes in three parts (see Figure 2b). In the first part (pre-training), we select the first 10 frames of the dataset and adopt a basin hopping algorithm that explores the high-dimensional parameter space by executing random walks.[45] Such a hopping algorithm is required for the given problem since the loss function is not globally convex and gradient methods become stuck in local minima. The hopping algorithm overcomes barriers in the loss function that hinder gradient-based optimization methods to find global convergence. After a configuration close to the global minimum of this small pre-training dataset is found, i.e., we obtained solid estimates of the model and orientation parameters, we use a gradient-based minimization method to optimize the parameter values for the pre-training set. In the second part of optimization, we fix the pre-trained model parameters and apply the basin hopping algorithm to each frame to obtain orientation parameter estimates that again are in the vicinity of the global solution of the entire dataset. Thus, we obtain good start values for the orientation parameter for each frame. In the third part, we feed the pre-trained model parameters together with the orientation parameters from the single frame estimates into a global gradient-based optimization, where all parameters are released to settle down at their optimum. Thus, we simultaneously optimize model and orientation parameters and find the MLE for the given measurement dataset. For this large set of parameters and iterations, we benefit from the linearity of the LL function that allows computing the global residual in a vectorized hence performant fashion.

Here we note that Figure 2b) shows only one possible solution to achieve global convergence of the optimization routine. Due to the nonlinearity of the model, in particular, due to the vanishing gradient for the sun being more than 90° apart from a single sensor viewing direction, gradient-based methods are prone to failure for most initial conditions. This is the reason why we use a stochastic search first to identify good initial conditions where gradient-based methods likely converge. Acting with such a stochastic search onto the entire dataset would give rise to hundreds of parameters which increase computational time exponentially up to unfeasible times until proper initial conditions would be found. This is the reason why the model training on a small part of the data is performed first and stochastic searches are carried out subsequently for roughly correct model parameters. Other optimization routines that include both stochastic and gradient components and that have an intrinsic memory for good parameter configurations could potentially do all these steps at once. In this context, we refer the interested reader to the methods of simulated annealing or adaptive memory programming for global optimization that are suited to solve complex optimization without well-defined gradients.[40] However, fine-tuning iteration parameters such as stochastic jump width, temperature decay, or convergence criteria and their interaction during optimization are hard to control in such a non-trivial optimization problem. The scheme in Figure 2b) allows keeping control and test possibilities along the way to the globally optimized solution.

In the second step, we calculate the posterior probability distribution using the affine invariant MCMC ensemble sampling starting from the gradient-optimized result. This method samples the true posterior probability distribution and asymptotically becomes the distribution for an infinite number of samples. We obtain parameter value distributions and correlations for the φ, θ, and β values of the single frames, i.e., marginalized over the distributions of the global parameters and independent for every single frame. As a final remark, we note that the inclusion of additional prior knowledge, e.g., about the limited pitch and roll rate of the payload during the μ-gravity time in form of Bayesian or Kalman filtering could stabilize the predictions and hence improve the obtained prediction accuracy.[46] However, the focus of this work is to investigate the solar position determination method and its accuracy without the use of other refinement techniques.

5. Results and Discussion

According to the Bayesian optimization method described earlier, we yield a full and consistent model and orientation parameter estimates for both, the Sun-only and Sun + Earth model for the entire data set as a result of the gradient-based global optimization. For the Sun-only model, α_c stabilized at around 65° for the pre-training, while it drifted to 90° during the global optimization. Consequently, we exclude it from the global optimization, thus the only varied model parameters are the L, σ, and solar position φ_i and θ_i in each frame i. For the Sun-only model, we attributed the drift of α_c toward high values to the incompleteness of the model. The pretraining data contains measurements of the phase of solar positions close to the equator, while the complete dataset also includes measurements during solar positions at high polar angles. In the latter case, the model sensor estimates underestimate the measured sensor response, since any additional radiation from Earth is not covered by the model. This naturally pushes the cutoff angle toward higher values to minimize residuals and prevented convergence. In **Figure 3** we show the results of the MLE estimation of the Sun-only model (dark-green & red lines) of the complete dataset. In addition, we show the solar trajectories, which are once directly derived from the Sun detected on the images of camera 1 and camera 2 (light green and cyan lines), and once computed from the integrated orientation solution, which is estimated by fusing the Earth's horizon and Sun detected on the camera images and the IMU measurements, and will be referred to as the fused Deutsches Zentrum für Luft- und Raumfahrt (DLR) trajectory in the following (dashed-gray lines). Camera 1 sees the

© 2022 The Authors. Solar RRL published by Wiley-VCH GmbH

2367198x, 2022, 11, Downloaded from https://onlinelibrary.wiley.com/doi/10.1002/solr.202200537 by Dtsch Zentrum F. Luft-U. Raum Fahrt In D. Helmholtz Gemein., Wiley Online Library on [09/02/2023]. See the Terms and Conditions (https://onlinelibrary.wiley.com/terms-and-conditions) on Wiley Online Library for rules of use; OA articles are governed by the applicable Creative Commons License

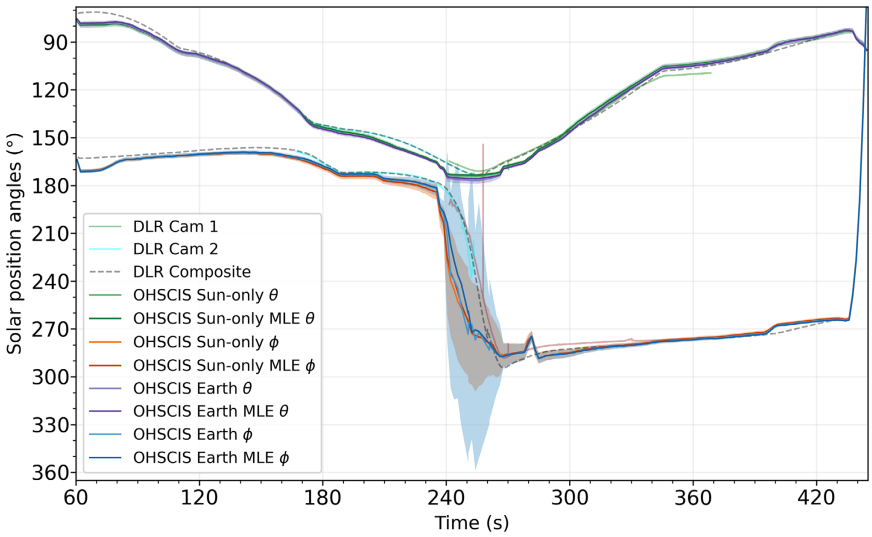

Figure 3. Solar position evolution for different models and techniques in the MORABA coordinate system. The solar position as derived from the Sun detected on the camera images is shown in light green and cyan, and the solar position as derived from the integrated orientation solution is shown as dashed-gray lines.[32] In the green and orange colors, we show the Sun-only θ and φ estimates and in the purple and blue colors, we show the Sun + Earth θ and φ estimates where the darker color depicts the maximum likelihood estimation (MLE) solution and the lighter color the median of the Monte-Carlo Markow-chain (MCMC) sampling distribution. In the lightly shadowed areas, we show 1-σ errors in the positioning estimation obtained from MCMC sampling. We note that at angles θ approaching 180°, small changes in solar positions convert into large uncertainties in φ estimations due to the nature of coordinate representation.

Sun in the central area of the image only between $T+240$ s and $T+370$ s, and camera 2 between $T+170$ s and $T+255$ s.

To summarize the solar trajectory during the flight of MAPHEUS-8, at the beginning of the dataset the solar position was located close to the equator and then wandered gradually to a polar position. It crossed the payload nadir and then wandered back to an equatorial position of a different azimuth. According to Braun et al., the error of the estimated orientation of the payload is assumed to be below 1.5° (3σ) in the period between $T+170$ s and $T+370$ s when at least one of the cameras sees the Sun and the estimated Sun direction vectors are directly used for aiding. In the initial period between $T+60$ s and $T+170$ s, neither camera sees the Sun, and the orientation is estimated by backpropagating the orientation solution of $T+170$ s using the IMU measurements, with the orientation error increasing due to the integration of IMU measurement errors over time. In the period between $T+370$ s and $T+445$ s, the orientation is estimated by forward propagating the orientation solution at $T+370$ s using IMU measurements. Interestingly, the OHSCIS result at $T+360$ s strongly supports the fused DLR trajectory with low deviation while it does not support the trajectory as derived from camera 1 only.

On top of the DLR trajectories, we present the OHSCIS solar positioning determination results from this work. We show the Sun-only model MLE trajectory and the MCMC sampling median and the central 1σ sampling distribution in green and orange for φ and θ respectively. For the MCMC sampling for the Sun-only model, we use 5 walkers and 10 000 steps and for the Sun + Earth model 20 walkers and 20 000 steps to better capture the richer probability landscape. To determine 1σ or 2σ from the sampling, we sort the samples along the axis (parameter) of interest. Then we select the lower and upper bound of the corresponding central 68% or 95% of the samples. Interestingly, the frame-to-frame differences for the OHSCIS determination method are very small for the majority of the data. This is a very encouraging result since the parameter solutions are independently estimated for each frame and this underlines that measurement signal-to-noise is high and the triangulation method reliable. The trajectory follows the fused DLR trajectory closely over very large portions of the entire flight with only small deviations. Focusing first on the phase with camera aiding between $\approx T+170$ s and $T+370$ s including the solar movement crossing nadir, the maximum measurement deviations of the fused DLR trajectory and the Sun-only model are $\Delta\theta \approx 5^{\circ}$. For $\Delta\varphi$ we find deviations that are reaching 30° at $T+240$-250 s, however, this is during times where θ approaches 180°, and thus small angular distances on the unit-sphere surface translate into large φ differences. The large φ deviations and also the φ uncertainty as derived from MCMC sampling are thus a direct consequence of the choice of the coordinate system and no intrinsic model weakness to determine the solar position. To underline this, we show the results of MCMC sampling for a phase of equatorial and polar solar position in **Figure 4**. During equatorial phases, the distribution width of θ and φ are small, covering around 3° for the 1 sigma range each. During polar phases, the θ sampling precision is still high (see also Figure S6, Supporting Information) but the φ angle distributions blow up toward the polar region, losing significance. In **Figure 5** we show the DLR and OHSCIS solar trajectories on an orientation sphere surface in Hammer-projection, which is an equal-area map projection with low distortions in the polar regions. This representation illustrates the magnitude of effective

© 2022 The Authors. Solar RRL published by Wiley-VCH GmbH

2367198x, 2022, 11, Downloaded from https://onlinelibrary.wiley.com/doi/10.1002/solr.202200537 by Dtsch Zentrum F. Luft-U. Raum Fahrt In D. Helmholtz Gemein., Wiley Online Library on [09/02/2023]. See the Terms and Conditions (https://onlinelibrary.wiley.com/terms-and-conditions) on Wiley Online Library for rules of use; OA articles are governed by the applicable Creative Commons License

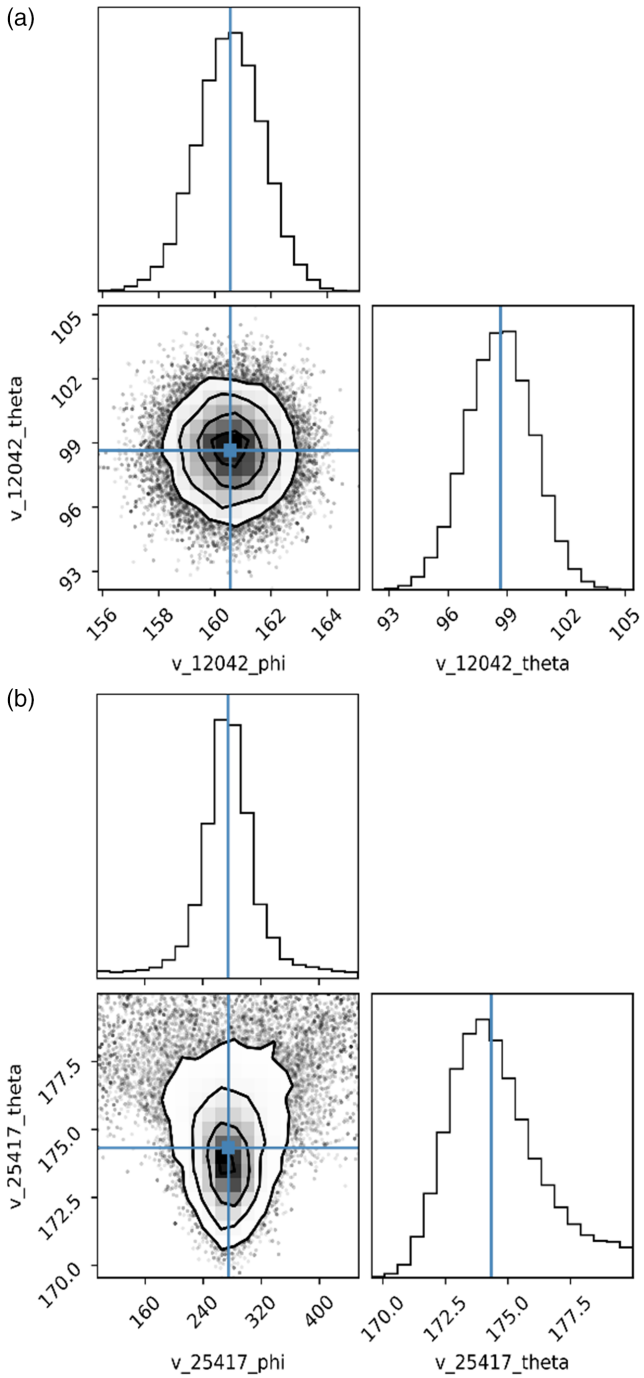

Figure 4. Corner plots of MCMC ensemble sampling results for the Sun-only model for: a) an equatorial solar position and b) the Sun in nadir position. Frame (b) is the darkest frame during the entire dataset. The MLE solution is shown in blue. For plots of more frames and plots of the Sun + Earth model, we refer the reader to Figure S6, Supporting Information. Note the automatic axes range adaption.

positioning deviations between the trajectories in a way that reduces misleading coordinate representation effects, especially for φ. If focusing on θ, we find exceptional agreement between the solar position estimates of the fused DLR trajectory and the OHSCIS model for measurements at times around $T + 170$ s and $T + 370$ s, i.e., during phases of rather equatorial Sun positions where the fused DLR trajectory is aided by camera measurements. In other words, when θ is not more than $\approx$150°, the orientation estimates of both methods are in excellent agreement. At higher polar angles, the corner plot contours become spread out toward higher polar angles, and the θ-angle distribution becomes skewed and generally less peaked. Still, the MCMC sampling appears to slightly underestimate the model uncertainty at such high polar angles. Likely, due to the rather weak sensor response, not-included noise effects or model imperfections become stronger during these times and cannot be fully captured by the model. This can be also seen with the noisy solar position estimates at very high polar angles. However, in this regard, MAPHEUS-8 produced an untypical dataset, because it is statistically unlikely that the Sun directly crosses the nadir.

The deviations outside the camera-aided periods between the two methods, i.e., in the beginning and end of the selected dataset appear to grow. For example, between $T + 60$ s and $T + 120$ s, the OHSCIS model experiences strong solar irradiance and thus the obtained solar positioning estimates shown in Figure 3a 1σ uncertainty of 2° and 3° for φ and θ, respectively (see also Figure 4 and Figure S6, Supporting Information for parameter distributions from sampling results). Here we note that the angle φ can be determined more precisely than θ at equatorial positions by the OHSCIS module since the light sensors react more strongly to a change in azimuthal solar position. The orientation accuracy of the fused DLR trajectory is expected to decrease with increasing period of time without camera image aiding due to the IMU-based backward and forward propagation, respectively. Thus, it is likely that deviations between the two models at such phases, especially for φ are dominantly attributed to the deviations of the fused DLR trajectory rather than deviations of the OHSCIS trajectory from the real solar trajectory.

To sum up the Sun-only model, the strong deviations in the orientation estimation of both methods at the beginning and end of the dataset are likely attributed to cumulative deviations in the propagation of the fused DLR trajectory. During and in the vicinity of phases that benefit from camera aiding (i.e., during times from $T + 100$ s until the end of the dataset, where propagation time is not exceeding around a minute), the maximum deviation of both methods is less than $\Delta\theta \approx 5°$ for $\theta \lesssim 150°$. Deviations of φ lie within a similar range, but strongly increase at high polar angles due to the coordinate system used.

In the refined model, we include a second, extended radiation source as described in the Radiation Model section to add the Earth as another component. In Figure 3, we added similarly the Sun + Earth model MLE trajectory and the MCMC sampling median and 1σ sampling distribution in purple and blue for φ and θ, respectively. In Figure S5, Supporting Information we show Earth's normal direction evolution over time as obtained from the MLE solution. At first sight, the estimated solar position trajectory from the composite model does not deviate significantly from the Sun-only model. Thus, the inclusion of Earth does not distort the solution for the solar position substantially. The global model parameter changed slightly (see **Table 1**). The solar brightness L is lowered by around 2%. The Earth's brightness reaches around 10% of the solar brightness, hence the

© 2022 The Authors. Solar RRL published by Wiley-VCH GmbH

2367198x, 2022, 11, Downloaded from https://onlinelibrary.wiley.com/doi/10.1002/solr.202200537 by Dtsch Zentrum F. Luft-U. Raum Fahrt In D. Helmholtz Gemein., Wiley Online Library on [09/02/2023]. See the Terms and Conditions (https://onlinelibrary.wiley.com/terms-and-conditions) on Wiley Online Library for rules of use; OA articles are governed by the applicable Creative Commons License

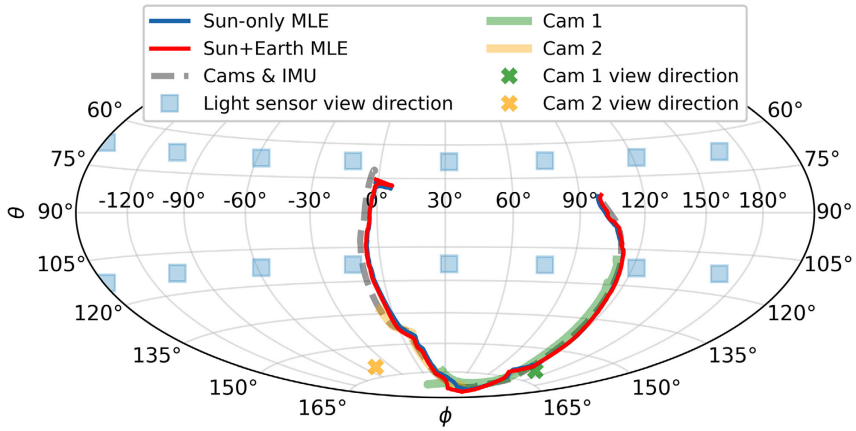

Figure 5. Hammer projection of the solar trajectories in the MORABA coordinate system. The movement of the solar position is counterclockwise. For additional orientation, we depict the view direction of the two opposite cameras and the light sensors. The dashed line shows the fused trajectory of Braun et al., in yellow and green we show their standalone camera-based solar position estimates. On top, we show the Organic and Hybrid Solar Cells In Space (OHSCIS) Sun-only MLE (blue) and the Sun + Earth MLE (red). In this representation, absolute trajectory deviations become better visible.

Table 1. Values of global model parameters and log-likelihood function.

	Sun brightness	Earth	Sigma	LL
Sun only	33 333	–	1110	32 692
Sun + Earth	32 703	3251	934	32 170

maximum Earth contribution is ≈3% of the maximum solar contribution for a single sensor. We don't analyze or interpret absolute brightness values more closely, since this general scaling value does only have a minor influence on the orientation estimation in single frames. Comparing the Sun + Earth model with the Sun-only model, the most pronounced changes are that differences in φ and θ estimations are largest during polar solar positions, well visible for θ in Figure 3. This is in agreement with our expectations since during this phase the solar irradiation onto the light sensors is weak, and the Earth component gains relative strength. Thus, the model is expected to be more strongly influenced by the Earth component. Second, it appears that corrective changes of the Sun + Earth model tend to be more pronounced in moments where the Sun-only model deviation from the fused DLR trajectory is larger. Interestingly, the Earth component shifts the estimated solar position systematically toward the fused DLR trajectory, effectively reducing deviations. The only exception is the θ estimation while the Sun crosses nadir, where the inclusion of Earth systematically increases θ to larger values. This effect is natural since, upon inclusion of the Earth, the Sun does not need to account for equatorial light scattered light from Earth anymore and thus moves freely to higher θ values. The apparent larger uncertainty of φ from MCMC sampling stems from the larger θ values. Apart from that, there is no significant reduction of the 1-σ band visible. The sigma parameter is reduced by 15%, showing that the inclusion of Earth, although a weak component, effectively reduces data–prediction discrepancies.

We expect to yield a stable cutoff angle after including the Earth radiation model. However, this does not turn out to be true: It still drifts toward higher values, consequently, we decide to exclude the sensor cutoff also for the Sun + Earth model. Possible explanations for the lack of stability for the refined model are, first of all, that the geometrical shadowing angle is not a constant value but rather has a directional dependency. To assess this effect more closely, we analyze the geometrical shadowing angles in polar and azimuthal directions using the computer-aided design of the OHSCIS module in Figure S7, Supporting Information. The geometrical shadowing angles in the four directions range from 55 to 90° for the sensor and the incidence angle to the glass normal direction range from 67.5 to 79°. Interestingly, the lower sensor cutoff angles coincide with higher glass incidence angles, effectively creating a smooth response leveling-off that renders the geometrical cutoff angle weakly constrained intrinsically. Second, the cutoff angle shows degeneration to a certain extent. It cuts off the sensor response at high angles where the effective response including glass transmission is already strongly reduced, limiting its total influence. Third, in the radiation model, we do not account for any stray light reaching the sensors, e.g., reflected from the hatch. Here, we note that such stray light does not influence the solar cell measurements since they are placed close to the window and their aperture masks efficiently shield possible stray light from entering. Lastly, we do not question our basic assumption of normally distributed measurement noise. Especially for processes like photon counting measurements of limited exposure usually follow Poisson count statistics. However, for sufficient exposure and count statistics, optimizations based on Poisson or Gaussian weighting deliver usually similar results. Poisson weighting would favor low-brightness measurements and thus improve e.g., the accuracy of Earth position determination. However, in this work, we set priority to precise Sun position estimation, i.e., to get reliable estimates for the strong radiation component that dominates the incident light on the light sensors for reliable irradiance determination for the solar cells.

From the solar position, we derive the irradiance onto each solar cell module for each time executing the following steps: For a given solar position, we calculate the fused silica glass

© 2022 The Authors. Solar RRL published by Wiley-VCH GmbH

2367198x, 2022, 11, Downloaded from https://onlinelibrary.wiley.com/doi/10.1002/solr.202200537 by Dtsch Zentrum F. Luft-U. Raum Fahrt In D. Helmholtz Gemein., Wiley Online Library on [09/02/2023]. See the Terms and Conditions (https://onlinelibrary.wiley.com/terms-and-conditions) on Wiley Online Library for rules of use; OA articles are governed by the applicable Creative Commons License

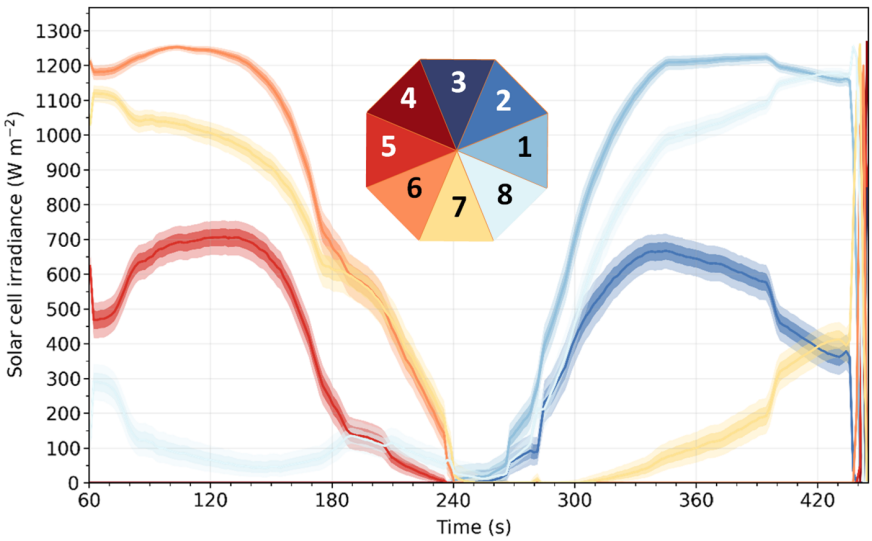

Figure 6. Irradiance evolution onto the solar cells during the flight for the eight different segments. The MCMC solar position sampling results are further processed to obtain the irradiance distributions similarly as in Figure 3. The colored lines represent the median of the irradiance distributions for each solar cell orientation, color-coded according to the octagonal inset. 1σ and 2σ bands are shown in addition. No geometrical shadowing effect is considered.

transmission for each window. For relative solar angles of less than 90°, we include the area projection effect as $\cos(\alpha)$. In this work, we use the AM0 irradiation strength of the solar constant of 1366.1 W m^{-2} according to the ASTM E-490 standard extraterrestrial spectrum.[34,35] It scales with fused silica glass transmission and angular projections, resulting in the effective irradiation onto each of the eight viewing directions of the different solar cell types. Note that here we do not include any geometrical shadowing effects that are expected to occur at high relative angles α or low irradiances (similar reasoning as for the light sensors, cf. Figure S7, Supporting Information). In **Figure 6**, we show the resulting reconstructed irradiance evolution during flight. The irradiance evolution can be considered as the final result to be used for further analysis of the solar cell performance parameters.

As expected from geometrical reasons, significant solar irradiance is present usually only for three segments at the same time. Comparing the apparent irradiance evolution in Figure 6 with the short-circuit current evolution of the solar cells in our previous work, Figure 6 confirms the conclusions drawn about the payload orientation evolution and the solar cell irradiance.[27] At the beginning of the μ-gravity phase, segment 6 receives solar irradiance close to AM0, i.e. 1200 W m^{-2} and above, and for segment 7 the solar irradiances are comparable to one sun. During payload alignment with the sun at around $T+250$ s, no direct sunlight irradiates the segments. At the end of the μ-gravity phase, segment 1 receives strong solar exposure. The equatorial crossing of the sun at $T+420$ s shows a special configuration of symmetry. At this crossing, segments 1 and 8, as well as segments 2 and 7 show the same irradiance values, respectively, where the latter values of ≈400 W m^{-2} correspond to a relative angle of around 67.5°. Focusing on the 1 and 2σ distribution bands, it becomes apparent that typically for high irradiance values, their uncertainties decrease and the estimates become more robust. This effect can be understood by having a closer look at Figure 1d, which shows the effective angular sensor response map including the fused silica glass transmission. The response map is relatively flat for small relative light source position angles to the fused silica glass normal, i.e., the sensor response is weakly sensitive to shifts of the solar position angle. The other way round, shifts of the solar position angle at equatorial solar positions do not translate into substantial shifts of derived irradiance, rendering this solar position estimation method robust for precise solar irradiance determination, especially for solar cells oriented in similar directions as the light sensors.

6. Conclusion

By using measurement data of 16 I2C ambient light sensors facing in different directions and refining a point source model to the data we obtain a precise solar positioning estimate for the entire μ-gravity time of the MAPHEUS-8 mission. Using MCMC methods, we sample the posterior likelihood distribution of the model parameters to derive estimates for orientation determination uncertainties. For equatorial solar positions, the method provides high accuracy within 3° uncertainty (1σ) that is comparable to or in phases more accurate than the camera-based estimates of Braun et al. Interestingly, our solution is closer to the fused trajectory of Braun et al. than to the standalone camera-based trajectories, validating their model that includes IMU measurements and propagation methods. Also for high solar inclinations, the optimized models give reasonable results with effective angular deviations that are largely below 10°. With our light sensor geometry, the effective field of view to determine the solar position encompasses practically the entire sky, even solar nadir (as well as zenith) crossings are registered by the

© 2022 The Authors. Solar RRL published by Wiley-VCH GmbH

2367198x, 2022, 11, Downloaded from https://onlinelibrary.wiley.com/doi/10.1002/solr.202200537 by Dtsch Zentrum F. Luft-U. Raum Fahrt In D. Helmholtz Gemein., Wiley Online Library on [09/02/2023]. See the Terms and Conditions (https://onlinelibrary.wiley.com/terms-and-conditions) on Wiley Online Library for rules of use; OA articles are governed by the applicable Creative Commons License

model. The inclusion of Earth as a second radiation component improves the model likelihood and estimates, bringing the trajectory closer to the fused trajectory of Braun et al. Our results show that first, our method is capable of improving the payload orientation estimation for sounding rocket flights, and second, that our method gives stable estimates for a broad range of solar positions with high accuracy in for payload orientations where the cameras cannot capture the Sun, making this a powerful complementary method. During flight, the payload covered many different orientations, making MAPHEUS-8 the ideal test case for this method. This will help to assess the quality of attitude determination in potential future flights with different orientation profiles.

The presented approach of using ambient light sensors together with light source modeling in combination with machine learning results in powerful results for simplistic sensors that are commercially broadly available. The presented system of light sensor parallelization is capable of predicting the solar position with comparable accuracy to advanced optical components and with very low power consumption and data storage requirements. It is not limited to space applications, instead, the concept can be transferred to terrestrial applications, more general to applications where attitude determination with respect to point-like and extended light sources is required. Using the trained model global parameters, together with a customized optimization routine, a handful of iteration steps for every single frame can determine the solar position, rendering these calculations computationally cheap. Hence, this method promises real-time solar triangulation with an accuracy of a few degrees, also with a limited computational effort, and for arbitrary sensor orientation configurations.

Using this technique and the chosen ambient light sensor geometry, we obtain highly precise solar irradiance estimates that allow reconstructing the incident solar power onto the differently oriented solar cells at each time during flight. Especially for strong solar illumination, such precise measurements are the basis for quantitative performance analysis for testing and qualifying novel thin film solar cell technologies for application in space and beyond.

Supporting Information

Supporting Information is available from the Wiley Online Library or from the author.

Acknowledgements

This work was supported by funding from the Deutsche Forschungsgemeinschaft (DFG, German Research Foundation) grant number Mu1487/22 and by International Research Training Group 2022 Alberta/Technical University of Munich International Graduate School for Environmentally Responsible Functional Materials (ATUMS) as well as from TUM.solar in the context of the Bavarian Collaborative Research Project "Solar Technologies Go Hybrid" (SolTech). The authors thank the department Mobile Rocket Base (MORABA) of the DLR Space Operations and Astronaut Training for the support and guidance during the project. The authors thank Dr. Benjamin Braun and Jochen Barf for exciting discussions about the different attitude determination methods.

Open Access funding enabled and organized by Projekt DEAL.

Conflict of Interest

The authors declare no conflict of interest.

Data Availability Statement

The data that support the findings of this study are available from the corresponding author upon reasonable request.

Keywords

attitude control, light sensors, machine learning, solar cells, space, triangulation

Received: June 15, 2022
Revised: July 29, 2022
Published online: September 1, 2022

[1] C. G. Reynolds, C. M. Green, V. Lomask, *Mil. Aff.* **1971**, *35*, 120.
[2] D. J. Flood, *Mod. Phys. Lett. B* **2001**, *15*, 561.
[3] A. Luque, S. Hegedus, *Handbook of Photovoltaic Science and Engineering*, 2nd ed., Wiley, Chichester, West Sussex **2011**, p. 32.
[4] J. Li, A. Aierken, Y. Liu, Y. Zhuang, X. Yang, J. H. Mo, R. K. Fan, Q. Y. Chen, S. Y. Zhang, Y. M. Huang, Q. Zhang, *Front. Phys.* **2021**, *8*, 631925.
[5] D. Cardwell, A. Kirk, C. Stender, A. Wibowo, F. Tuminello, M. Drees, R. Chan, M. Osowski, N. Pan, in *2017 IEEE 44th Photovoltaic Specialists Conf. (PVSC)*, IEEE, Piscataway, NJ June 2017, pp. 3511–3513.
[6] N. S. Fatemi, H. E. Pollard, H. Q. Hou, P. R. Sharps, in *Conf. Record of the Twenty-Eighth IEEE Photovoltaic Specialists Conf.- 2000 (Cat. No.0°CH37036)*, IEEE, Piscataway, NJ September 2000, pp. 1083–1086.
[7] S. Surampudi, J. Blosiu, P. Stella, J. Elliott, J. Castillo, T. Yi, J. Lyons, M. Piszczor, J. McNatt, C. Taylor, E. Gaddy, S. Liu, E. Plichta, C. Iannello, *Solar Power Technologies for Future Planetary Science Missions*, Tech. Rep., NASA **2017**, JPL D-10136.
[8] M. A. Green, E. D. Dunlop, J. Hohl-Ebinger, M. Yoshita, N. Kopidakis, X. Hao, *Prog. Photovoltaics Res. Appl.* **2022**, *30*, 3.
[9] NREL, Best Research-Cell Efficiencies, https://www.nrel.gov/pv/cell-efficiency.html, (accessed: June 2022).
[10] J. Y. Kim, J.-W. Lee, H. S. Jung, H. Shin, N.-G. Park, *Chem. Rev.* **2020**, *120*, 7867.
[11] A. Armin, W. Li, O. J. Sandberg, Z. Xiao, L. Ding, J. Nelson, D. Neher, K. Vandewal, S. Shoaee, T. Wang, H. Ade, T. Heumüller, C. Brabec, P. Meredith, *Adv. Energy Mater.* **2021**, *11*, 2003570.
[12] I. Massiot, A. Cattoni, S. Collin, *Nat Energy* **2020**, *5*, 959.
[13] W. Huang, Z. Jiang, K. Fukuda, X. Jiao, C. R. McNeill, T. Yokota, T. Someya, *Joule* **2020**, *4*, 128.
[14] M. Kaltenbrunner, M. S. White, E. D. Głowacki, T. Sekitani, T. Someya, N. S. Sariciftci, S. Bauer, *Nat. Commun.* **2012**, *3*, 770.
[15] M. Kaltenbrunner, G. Adam, E. D. Głowacki, M. Drack, R. Schwödiauer, L. Leonat, D. H. Apaydin, H. Groiss, M. C. Scharber, M. S. White, N. S. Sariciftci, S. Bauer, *Nat. Mater.* **2015**, *14*, 1032.
[16] S. Kang, J. Jeong, S. Cho, Y. J. Yoon, S. Park, S. Lim, J. Y. Kim, H. Ko, *J. Mater. Chem. A* **2019**, *7*, 1107.
[17] Y. Hu, T. Niu, Y. Liu, Y. Zhou, Y. Xia, C. Ran, Z. Wu, L. Song, P. Müller-Buschbaum, Y. Chen, W. Huang, *ACS Energy Lett.* **2021**, *6*, 2917.

© 2022 The Authors. Solar RRL published by Wiley-VCH GmbH

2367198x, 2022, 11, Downloaded from https://onlinelibrary.wiley.com/doi/10.1002/solr.202200537 by Dtsch Zentrum F. Luft-U. Raum Fahrt In D. Helmholtz Gemein., Wiley Online Library on [09/02/2023]. See the Terms and Conditions (https://onlinelibrary.wiley.com/terms-and-conditions) on Wiley Online Library for rules of use; OA articles are governed by the applicable Creative Commons License

[18] K. S. Wienhold, V. Körstgens, S. Grott, X. Jiang, M. Schwartzkopf, S. V. Roth, P. Müller-Buschbaum, *Sol. RRL* **2020**, *4*, 2000086.
[19] L.-H. Chou, J. M. W. Chan, C.-L. Liu, *Sol. RRL* **2022**, *6*, 2101035.
[20] X. Meng, X. Tian, S. Zhang, J. Zhou, Y. Zhang, Z. Liu, W. Chen, *Sol. RRL* **2022**, *6*, 2200280.
[21] D. Pérez-del-Rey, C. Dreessen, A. M. Igual-Muñoz, L. van den Hengel, M. C. Gélvez-Rueda, T. J. Savenije, F. C. Grozema, C. Zimmermann, H. J. Bolink, *Sol. RRL* **2020**, *4*, 2000447.
[22] S. Bailey, G. Landis, R. Raffaelle, *Proc. of the 6th European Conf. on Space Power, ESA SP-502*, Porto, Portugal **2002**, p. 9.
[23] J. Yang, Q. Bao, L. Shen, L. Ding, *Nano Energy* **2020**, *76*, 105019.
[24] S. Guo, C. Brandt, T. Andreev, E. Metwalli, W. Wang, J. Perlich, P. Müller-Buschbaum, *ACS Appl. Mater. Interfaces* **2014**, *6*, 17902.
[25] I. Cardinaletti, T. Vangerven, S. Nagels, R. Cornelissen, D. Schreurs, J. Hruby, J. Vodnik, D. Devisscher, J. Kesters, J. D'Haen, A. Franquet, V. Spampinato, T. Conard, W. Maes, W. Deferme, J. V. Manca, *Sol. Energy Mater. Sol. Cells* **2018**, *182*, 121.
[26] D. Schreurs, S. Nagels, I. Cardinaletti, T. Vangerven, R. Cornelissen, J. Vodnik, J. Hruby, W. Deferme, J. V. Manca, *J. Mater. Res.* **2018**, *33*, 1841.
[27] L. K. Reb, M. Böhmer, B. Predeschly, S. Grott, C. L. Weindl, G. I. Ivandekic, R. Guo, C. Dreißigacker, R. Gernhäuser, A. Meyer, P. Müller-Buschbaum, *Joule* **2020**, *4*, 1880.
[28] L. K. Reb, M. Böhmer, B. Predeschly, S. Grott, C. Dreißigacker, J. Drescher, A. Meyer, P. Müller-Buschbaum, *Rev. Sci. Instrum.* **2021**, *92*, 74501.
[29] Y. Tu, G. Xu, X. Yang, Y. Zhang, Z. Li, R. Su, D. Luo, W. Yang, Y. Miao, R. Cai, L. Jiang, X. Du, Y. Yang, Q. Liu, Y. Gao, S. Zhao, W. Huang, Q. Gong, R. Zhu, *Sci. China Phys. Mech. Astron.* **2019**, *62*, 974221.
[30] R. Guo, D. Han, W. Chen, L. Dai, K. Ji, Q. Xiong, S. Li, L. K. Reb, M. A. Scheel, S. Pratap, N. Li, S. Yin, T. Xiao, S. Liang, A. L. Oechsle, C. L. Weindl, M. Schwartzkopf, H. Ebert, P. Gao, K. Wang, M. Yuan, N. C. Greenham, S. D. Stranks, S. V. Roth, R. H. Friend, P. Müller-Buschbaum, *Nat Energy* **2021**, *6*, 977.
[31] A. Awasthi, A. K. Shukla, S.R. Murali Manohar, C. Dondariya, K. N. Shukla, D. Porwal, G. Richhariya, *Energy Rep.* **2020**, *6*, 392.
[32] B. Braun, J. Barf, *CEAS Space J.* **2022**, https://link.springer.com/article/10.1007/s12567-022-00461-0.
[33] Rohm Co., Ltd., Digital 16bit Serial Output Type Ambient Light Sensor IC, https://www.mouser.com/datasheet/2/348/bh1750fvi-e-186247.pdf, (accessed: June 2022).
[34] M. A. Green, *Prog. Photovoltaics: Res. Appl.* **2012**, *20*, 954.
[35] NREL, 2000 ASTM Standard Extraterrestrial Spectrum Reference E-490-00, https://www.nrel.gov/grid/solar-resource/spectra-astm-e490.html, (accessed: July 2022).
[36] Heraeus Quarzglas GmbH & Co. KG, Quartz Glass for Optics, https://www.heraeus.com/media/media/hca/doc_hca/products_and_solutions_8/optics/Data_and_Properties_Optics_fused_silica_EN.pdf, (accessed: June 2022).
[37] G. van Rossum, *The Python Language Reference*, 3rd ed., Python Software Foundation, SoHo Books, Hampton, NH, Redwood City **2010**, p. 126.
[38] C. R. Harris, K. J. Millman, S. J. van der Walt, R. Gommers, P. Virtanen, D. Cournapeau, E. Wieser, J. Taylor, S. Berg, N. J. Smith, R. Kern, M. Picus, S. Hoyer, M. H. van Kerkwijk, M. Brett, A. Haldane, J. F. Del Río, M. Wiebe, P. Peterson, P. Gérard-Marchant, K. Sheppard, T. Reddy, W. Weckesser, H. Abbasi, C. Gohlke, T. E. Oliphant, *Nature* **2020**, *585*, 357.
[39] M. Newville, T. Stensitzki, D. B. Allen, A. Ingargiola, LMFIT: Non-Linear Least-Square Minimization and Curve-Fitting for Python, Zenodo **2014**.
[40] P. Virtanen, R. Gommers, T. E. Oliphant, M. Haberland, T. Reddy, D. Cournapeau, E. Burovski, P. Peterson, W. Weckesser, J. Bright, S. J. van der Walt, M. Brett, J. Wilson, K. J. Millman, N. Mayorov, A. R. J. Nelson, E. Jones, R. Kern, E. Larson, C. J. Carey, İ. Polat, Y. Feng, E. W. Moore, J. VanderPlas, D. Laxalde, J. Perktold, R. Cimrman, I. Henriksen, E. A. Quintero, C. R. Harris, et al., *Nat. Methods* **2020**, *17*, 261.
[41] Jeff Reback, Jbrockmendel, W. McKinney, J. Van den Bossche, T. Augspurger, M. Roeschke, S. Hawkins, P. Cloud, Gfyoung, Sinhrks, P. Hoefler, A. Klein, T. Petersen, J. Tratner, C. She, W. Ayd, S. Naveh, J.H.M. Darbyshire, M. Garcia, R. Shadrach, J. Schendel, A. Hayden, D. Saxton, M. E. Gorelli, F. Li, M. Zeitlin, V. Jancauskas, A. McMaster, T. Wörtwein, P. Battiston, pandas-dev/pandas: Pandas 1.4.2, Zenodo **2022**.
[42] J. D. Hunter, *Comput. Sci. Eng.* **2007**, *9*, 90.
[43] J. Goodman, J. Weare, *CAMCoS* **2010**, *5*, 65.
[44] D. Foreman-Mackey, D. W. Hogg, D. Lang, J. Goodman, *Publ. Astron. Soc. Pac.* **2013**, *125*, 306.
[45] B. Olson, I. Hashmi, K. Molloy, A. Shehu, *Adv. Artif. Intell.* **2012**, *2012*, 1.
[46] S. Sarkka, *Bayesian Filtering and Smoothing*, Cambridge University Press, Cambridge **2013**, p. 232.

© 2022 The Authors. Solar RRL published by Wiley-VCH GmbH

2367198x, 2022, 11, Downloaded from https://onlinelibrary.wiley.com/doi/10.1002/solr.202200537 by Dtsch Zentrum F. Luft-U. Raum Fahrt In D. Helmholtz Gemein., Wiley Online Library on [09/02/2023]. See the Terms and Conditions (https://onlinelibrary.wiley.com/terms-and-conditions) on Wiley Online Library for rules of use; OA articles are governed by the applicable Creative Commons License